Catalysis Science & Technology

ROYAL SOCIETY OF CHEMISTRY

PAPER

View Article Online
View Journal | View Issue

Cite this: *Catal. Sci. Technol.*, 2020, **10**, 4362

Catalytic performance and stability of Fe-doped CeO_2 in propane oxidative dehydrogenation using carbon dioxide as an oxidant†

Hedun Wang and George Tsilomelekis *

Received 23rd March 2020,
Accepted 1st June 2020

DOI: 10.1039/d0cy00586j

rsc.li/catalysis

Propane oxidative dehydrogenation (ODH) in the presence of CO_2 was investigated over a series of Fe-doped CeO_2 catalysts. The well-recognized properties of cerium oxide materials regarding improved oxygen mobility and oxygen storage capacity (OSC) were utilized towards the synthesis of stable catalytic systems. The iron–cerium oxide solid solution catalysts with an Fe dopant content from 1% up to 15% were successfully synthesized *via* a co-precipitation method and calcined at 873 K. It was confirmed by XRD and Raman characterization that all samples featured a single cerianite crystalline phase with periodic lattice Ce ions substituted by Fe ions, with no hematite phase identified. Initial screening of catalytic behavior showed that the propane ODH pathway was enhanced at high Fe/Ce ratio while propane cracking was suppressed. Stable propane conversion and propylene selectivity for up to 20 hours were achieved for the synthesized catalysts with moderate Fe loading. *Ex situ* Raman, XPS and STEM were applied to analyze post-reaction catalysts and confirmed that deactivation occurring over low Fe catalysts resulted from coke deposition on the surface, while CeO_2 sintering and Fe migration to form nanocrystals were the primary deactivation reasons for high Fe loading catalysts.

Introduction

Propylene is undoubtedly among the most important and fastest growing in demand petrochemicals. Although fluid catalytic cracking (FCC) as well as steam cracking processes are still widely utilized, research efforts have been placed in developing new technologies that maximize propylene production while addressing the big gap between supply and demand. Vast availability of low molecular weight alkanes due to the recent shale gas revolution is considered as a game-changing opportunity towards the potential development of 'on-purpose' production processes. Propane direct dehydrogenation (DH) as well as oxidative dehydrogenation (ODH) have attracted worldwide academic and industrial interest, but both suffer from limitations that have been reviewed extensively elsewhere.[1–3]

Propane DH is an endothermic reaction and thus high temperatures are required to achieve acceptable olefin yields.

$$C_3H_8 \rightarrow C_3H_6 + H_2,\ \Delta H = +124.3\ \text{kJ mol}^{-1} \quad (1)$$

The CATOFIN® dehydrogenation process[4,5] provides 850 000 MTA (million metric tons annually) of propylene with a minimum purity of 99.5% and is based on chromium oxide supported on activated alumina. The toxicity of chromium-based catalysts, especially the hexavalent chromium species that initially dominate the surface of the catalyst, is an important issue. The Oleflex dehydrogenation process[4,5] relies on the traditional Pt/Sn catalytic system to produce polymer grade propylene. The high operating temperature as well as the cost of the Pt catalysts comprise the main drawbacks. In addition, the reaction is usually accompanied by catalyst deactivation due to coke formation and spatial separation of Pt–Sn species thus highlighting the stability of catalysts used among the major botlenecks.[6,7]

On the other hand, although the exothermic character of propane ODH with O_2 has the potential to significantly reduce the reaction temperature, the fate of the desired propylene is difficult to control due to unavoidable combustion of propane as well as of propylene to carbon monoxide and/or dioxide thus significantly lowering propylene selectivity. Even though there is very rich literature on various catalytic systems (*e.g.* metals, transition metal oxides, rare-earth metal oxides, metal carbides, supported alkali oxides and supported alkali chlorides), the lack of suitable catalysts that exhibit high activity while maintaining promising olefin selectivity hampers potential endeavors for large scale commercialization.

Department of Chemical and Biomolecular Engineering, Rutgers, The State University of New Jersey, USA. E-mail: gt241@soe.rutgers.edu

† Electronic supplementary information (ESI) available. See DOI: 10.1039/d0cy00586j

The aforementioned competitive reaction network due to overoxidation of paraffins and/or olefins can be suppressed by replacing oxygen with a weak oxidant, such as carbon dioxide.[8] The use of CO_2 as a soft oxidant, an alternative to oxygen, has the potential to i) avoid deep oxidation of alkanes/alkenes, ii) reduce coke formation and iii) favor propane conversion due to participation of the produced hydrogen in the reverse water–gas shift (RWGS) reaction.

$$CO_2 + H_2 \rightleftharpoons CO + H_2O \quad (2)$$

In recent years, a large variety of metal oxide catalysts have been explored in propane ODH with CO_2 with dispersed chromium oxide species to show great potential as active sites towards high conversion and selectivity. XANES and XPS results for spent catalysts have shown that during the reaction process,[9–11] Cr^{6+} undergoes a rapid reduction to Cr^{3+}/Cr^{2+}, which is crucial for catalytic activity.[12–16] With CO_2 being a soft oxidant, it was found that reduced Cr species can be partially re-oxidized to higher oxidative states. Although promising initial propylene yield was achieved, Cr-based catalysts suffer from severe and rapid deactivation within a short time, regardless of sample preparation, reaction conditions and reactor design. The proposed reasons behind the severe deactivation include potential coking,[11,13,17,18] collapse of the catalyst mesoporous structure,[17] agglomeration of reduced Cr to Cr_2O_3,[19] *etc.* In addition, Zhang *et al.* have suggested the reduction of Cr(VI) to Cr(III)/Cr(II) as the main reason behind deactivation.[20]

Pioneering work by the research group of JG Chen has provided molecular level understanding on light alkane CO_2 assisted ODH over non-precious metal (Fe–Ni) and precious metal (Fe–Pt, Ni–Pt) over CeO_2.[21–26] Recently, the effect of oxide supports was also investigated by the same research group highlighting CeO_2 as the most promising support[26] due to its ability to activate CO_2 *via* direct C=O bond scission. Olefin selectivity was found to depend on competitive reaction pathways such as ODH, reverse water gas shift and alkane dry reforming that can be tuned *via* rational selection of the bimetallic composition of active sites. DFT calculations suggested that the Fe–Ni surface favors C–H bond scissoring while the Pt-determined surface favors C–C cleavage. Additional evidence from EDS and TGA of spent Fe–Ni catalyst deactivation showed small regions of higher Fe content as compared to those of the fresh catalyst thus excluding coking as the main deactivation reason.

In this work, we report a series of Fe doped CeO_2 as catalysts that show enhanced stability and promising catalytic performance for propane oxidative dehydrogenation using CO_2 as a soft oxidant. The well-reported oxygen mobility and oxygen storage capacity (OSC) of ceria based catalysts sets the foundation and main hypothesis of this work towards the formation of stable surface active sites.[27,28] To that end, we introduce Fe^{3+}, which is proved to be active for propane dehydrogenation[23,29,30] as well as CO_2 activation,[21,23,31] into a ceria lattice with a series of Fe/Ce molar ratios.

Experimental

Materials and synthesis of the catalysts

$Ce(NO_3)_3{\cdot}6H_2O$ (99.99%) and $Fe(NO_3)_3{\cdot}9H_2O$ (99.95%) were purchased from Sigma Aldrich and used without further purification. A series of Fe-doped ceria materials as bimetallic oxide catalysts (xFeCeO$_2$$T$, x indicates the molar percentage of Fe over Ce atoms; T indicates the calcination temperature in degree Celsius) were prepared batchwise *via* a co-precipitation method, as reported elsewhere.[32–34] In a typical synthesis, a pre-calculated amount of precursor solutions was mixed and heated up to 343 K under stirring. NH_4OH (Sigma Aldrich 30%) was added dropwise as a precipitating agent by elevating the solution pH value. The mixed precursor solution was kept stirring for 1 hour when the pH was adjusted to around 7–8. An additional ammonium solution was added dropwise until pH reached 10.5. The mixture was kept at 343 K for 24 hours. The precipitation mixture was then filtered, washed thoroughly with 1 L DI water and 200 ml pure ethanol, and then dried at 110 °C overnight.

Determination of calcination temperature

Calcination temperature is crucial for phase transformation and crystalline growth, as well as removal of surface hydroxyl groups and possible carbon-based organics. Fe-doped ceria from the same synthesis batch were calcined at different temperatures and characterized by BET, Raman and XRD. As shown in the ESI,† (Fig. S1, Table S1) calcination at 600 °C is beneficial in the following aspects: higher specific surface area and formation of an Fe–Ce solid solution rather than two separated cerianite–hematite phases are achieved. Although it has been shown in the open literature that 450 °C is a suitable temperature in terms of formation of Fe–Ce solid solution structure,[35] the actual reaction conditions (as shown later) for CO_2 assisted propane ODH require a higher temperature (550–600 °C) and as a consequence, all samples studied for catalytic tests were calcined at 600 °C as an optimal temperature.

Characterization methods

All prepared samples were thoroughly characterized prior to the catalytic performance tests in order to obtain their physicochemical properties.

BET analysis

BET surface area measurements were conducted with a Micromeritics TriStar 3000 (Serial # 2111) system. Typically, around 30 mg of catalyst was loaded into a BET tube and degassed at 150 °C for 8 hours prior to BET analysis in order to completely remove chemisorbed water from the sample surface. Thirteen points were collected within 0.05 to 0.3 P/P_0 with a 0.02 increment.

X-ray powder diffraction (XRD)

XRD analysis was performed with a PANalytical Philips X'Pert X-ray diffractometer to determine the crystallinity and phase

composition. The XRD instrument is equipped with a CuKα source at 40 kV and 40 mA and angular incidence 2θ between 20° and 90° with 0.05° steps and 4.0 s per step. The phase composition was analysed by whole pattern fitting (WPF) refinement 2-phase analysis with a target relative error R% below 15%. Silicon was used as an external standard reference to determine any possible peak shift.

Raman spectroscopy

Raman spectra of the samples were collected with a Horiba Scientific LabSpec HR Evolution Raman spectrometer cooled with a Synapse CCD detector (−70 °C). The laser line used (532 nm solid-state, 80 mw) was directed on the sample and focused by using a 50× long working distance objective. The power of the laser was kept at a low value to avoid overheating by using a neutral density filter (5%). The acquisition time was 30 seconds with a total of twenty accumulations.

X-ray photoelectron spectroscopy (XPS)

X-ray photoelectron spectroscopy analysis was performed with a 180° double focusing hemispherical analyzer and Al-Kα X-ray monochromatic source (400 mm analysis spot size). The post-reaction catalysts were sieved with a 325 mesh. All samples were exposed to air in a sufficiently long time before analysis.

Scanning transmission electron microscopy (STEM)

Both the imaging and electron energy loss (EEL) data were acquired using a Nion UltraSTEM™ 100. The microscope was operated at 60 kV with a probe convergence semi-angle of 35 mrad and an energy loss collection semi-angle of 34 mrad. The EEL spectrum imaging (SI) data were processed using Hyperspy1, a python-based microscopy analysis package. After background removal, the intensity of each element in the SI data was normalized to its maximum value in the SI map such that one can visualize the spatial distribution of the elements in the acquired area.

Catalytic performance test

The catalytic activity was evaluated in a fixed bed quartz tube reactor (4 mm ID) packed with 200 mg catalyst diluted in 1000 mg of quartz sand (ACROS Organics 40–100 mesh). Reactant co-feed consists of propane (Airgas, 50% in nitrogen), CO2 (Airgas, BD) and N_2 (Airgas, UHP). The reactant mixture was fed into the reactor (Scheme 1) with a flowrate varying from 10 to 30 mL min^{-1} with 5% propane and 5% carbon dioxide in balance nitrogen, unless otherwise stated. The catalyst was preheated in oxygen (Airgas, UHP) with 5 K min^{-1} until the desired reaction temperature and kept in the same gas environment for 30 min to ensure the presence of the fully oxidized catalyst. The catalysts were evaluated for the ODH reaction in the temperature range of 450 to 600 °C and at atmospheric pressure. The outlet stream

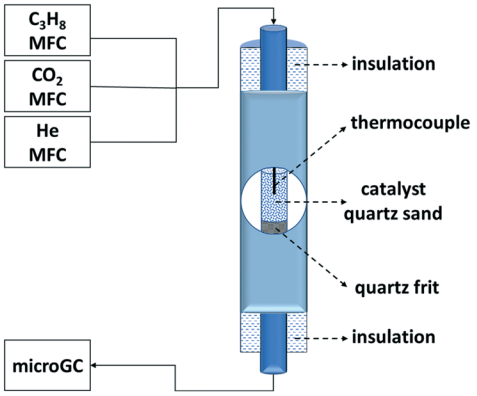

Scheme 1 Experimental setup of the fixed-bed reactor used for the catalytic measurements.

was analysed with an in-line microGC (Agilent 490) equipped with an MS5A column (for CH_4, CO and H_2) and a PoraPlot Q column (for CO_2, C_2H_4, C_2H_6, C_3H_6, and C_3H_8). Calculations of reactant conversion, selectivity and yield to main products and by-products were estimated as follows:

$$X_{C_3H_8} = \frac{F_{in,C_3H_8} - F_{out,C_3H_8}}{F_{in,C_3H_8}} \times 100\%$$

$$S_{C_3H_6} = \frac{F_{C_3H_6}}{F_{in,C_3H_8} - F_{out,C_3H_8}} \times 100\%$$

$$S_{C_xH_y} = \frac{\frac{x}{3} \times F_{C_xH_y}}{F_{in,C_3H_8} - F_{out,C_3H_8}} \times 100\%$$

$$\text{Yield} = X_{C_3H8} \times S_{C_3H6}$$

Results and discussion

Structural implications of Fe-doped CeO_2 catalysts

X-ray diffractograms of the various Fe-doped ceria materials are shown in Fig. 1. Upon calcination at 600 °C, all the materials show that cerianite is the main crystalline phase (reference cerianite phase lines are also included). As compared to the reference cerianite, all diffraction peaks of the Fe-doped ceria samples shift to higher Bragg angles underscoring the formation of Fe–Ce solid solution, where Ce^{4+} cations are partially substituted by smaller Fe^{3+} ions inside the cubic ceria structure.[27] The small shift as well as observed broadening of the diffraction peaks also indicate the possible changes of the crystallite sizes of cubic CeO_2; however, the average crystallite size of cubic CeO_2 as estimated from the corresponding (111) diffraction peak by means of the Debye–Scherrer equation (see ESI,† Table S1) appears to be within 8–12 nm without a monotonic behaviour across different samples. In addition, this type of partial substitution of Ce ions has the potential to result in different local environments of the oxygen atoms such as oxygen from the main ceria lattice phase, oxygen surrounded by Ce/Fe cations (Ce-rich) and/or oxygen surrounded by Fe/Ce

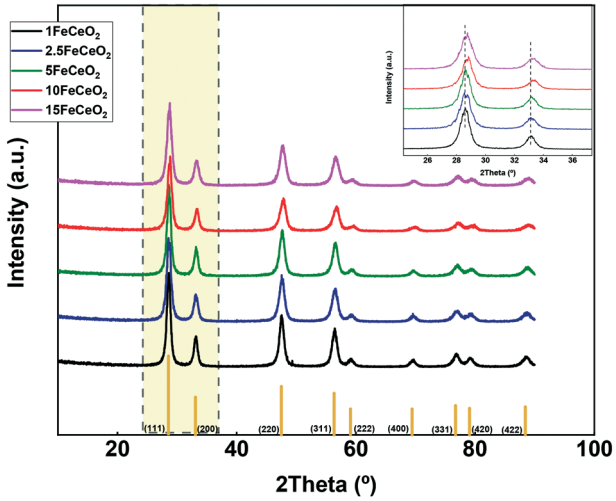

Fig. 1 XRD patterns of the catalytic materials synthesized with various Fe/Ce molar ratios. CeO_2 reference is also shown for comparison.

cations (Fe-rich).[36] The diverse nature of oxygen atoms and/or vacancies created within the surface of CeO_2 have been highlighted as important active sites for propane activation. It is worth mentioning here that the crystalline hematite (α-Fe_2O_3) phase was not detected by XRD for any of the samples tested indicating good dispersion of Fe in the ceria lattice. The possibility of very small α-Fe_2O_3 crystals that lie below the detection limit of XRD cannot be excluded.

Catalytic evaluation

Initial screening of xFeCeO$_2$ catalysts. In Fig. 2a, we present the catalytic evaluation screening, as referred to propane conversion and olefin selectivity for all catalysts synthesized. The data reported in Fig. 2 pertain to initial reaction conditions, 20 ml min^{-1} total flow (w/F = 0.6 g s cc^{-1}) and constant temperature at 550 °C. The data collected for commercial CeO_2 and Fe_2O_3 as well as their physical mixture (Fe_2O_3/CeO_2 = 1 : 20 molar ratio) are also included for comparison. The commercial CeO_2 shows very low conversion, less than 5%, with a propylene selectivity reaching around 40%. Fe_2O_3 shows slightly higher propane conversion while the propylene selectivity decreased dramatically due to the formation of carbon oxides as discussed later. A physical mixture of the commercial CeO_2 and Fe_2O_3 resulted in almost double propane conversion (as compared to pure CeO_2) with the propylene selectivity reaching almost that of pure CeO_2. Although moderate temperature treatment (close to the reaction temperature, *i.e.* 550 °C) of CeO_2 and Fe_2O_3 physical mixtures does not alter significantly the local structure of the individual oxides, it is reported that the reducibility and overall redox properties can be enhanced just through their physical contact.[37] The incorporation of a small amount of Fe (1FeCeO$_2$) in the ceria structure as a dopant leads to a significant increase in propane conversion while the propylene selectivity slightly decreases as compared to that of pure CeO_2. Upon increasing of the Fe content, a monotonic increasing trend in propane conversion was observed from 6.5% (1FeCeO$_2$) to 21.5% (15FeCeO$_2$). Interestingly, although the conversion increases, the same behaviour was observed for the selectivity towards propylene, reaching a maximum of around 47% for the 10FeCeO$_2$ catalyst. The increase in propane conversion can be partially associated with the increase in the surface area of the catalysts (see Table S1 of the ESI†). A maximum in propylene selectivity and propane conversion is achieved

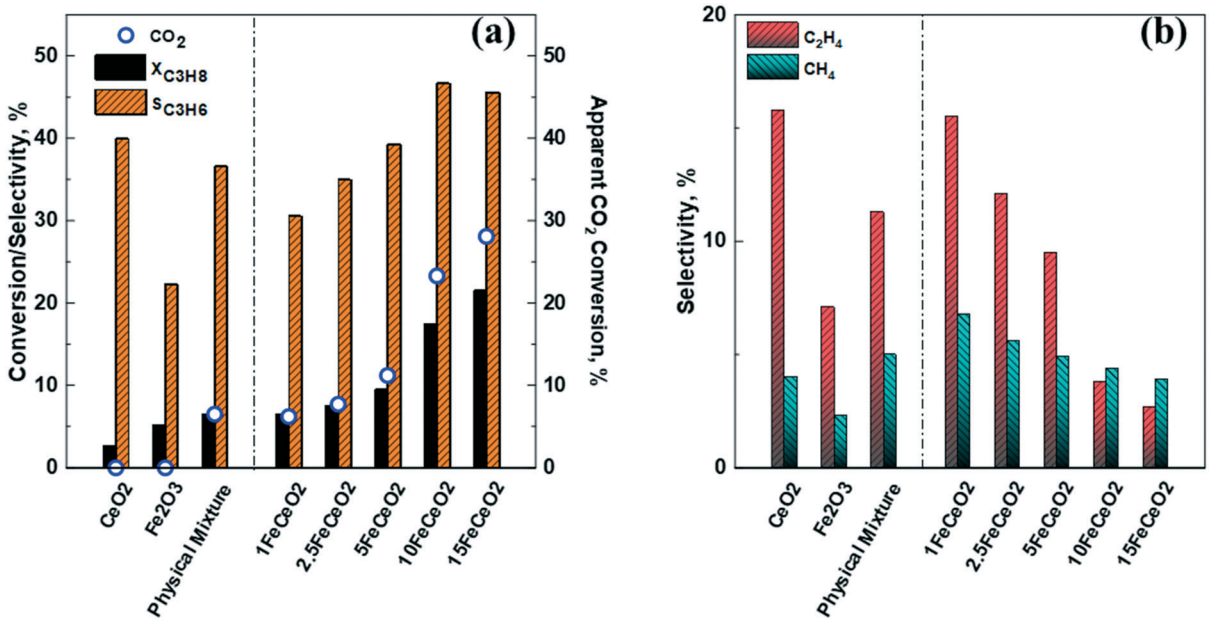

Fig. 2 (a) Propane and apparent CO_2 conversion as well as propylene selectivity and (b) selectivity to ethylene and methane of all synthesized catalysts. Data pertain to initial reaction conditions, 20 ml min^{-1} total flow (w/F = 0.6 g s cc^{-1}) and constant temperature at 550 °C.

between $10FeCeO_2$ and $15FeCeO_2$ with the initial yield reaching ~10% for the $15FeCeO_2$ catalyst at 550 °C. Besides the slightly higher surface area, the results suggest that there is a promotional effect of Fe as a dopant on the activity of C–H bond activation. This effect can be associated with the relative changes induced in active species with different local oxygen environments. As Fan *et al.*[36] demonstrated in a recent DFT study of ethylbenzene ODH on $ZrCeO_x$, the C–H bond activation is positively correlated with charge transferred from adsorbed hydrocarbon species to the catalyst surface. It is likely that higher Fe concentration benefits the formation of Fe-rich oxygen sites rather than Ce-rich or Ce lattice oxygen species, which in turn results in advantages from two different aspects: lowering of the reaction activation energy barrier and favoring the formation of oxygen vacancies in the ceria surface lattice. The former has the potential to improve the catalytic activity, *i.e.* propane conversion, while the latter is observed to be closely associated with propylene selectivity, which is discussed in the later section.

In Fig. 2b, the selectivity patterns to methane and ethylene are also shown. A monotonic decrease in the formation of methane and ethylene is clear as more Fe is incorporated in the catalyst structure. The most straightforward propane conversion pathway towards ethylene and methane is the catalytic cracking which stoichiometrically results in a 1 : 1 molar ratio between these hydrocarbon products:

$$C_3H_8 \rightarrow CH_4 + C_2H_4 \quad (3)$$

In low Fe content catalysts (up to $5\%FeCeO_2$) the molar ratio of methane-to-ethylene is very close to 1 (see Fig. S2 of ESI†), indicating that selectivity loss is associated with propane cracking. On the other hand, the methane-to-ethylene molar ratio increased by two-fold over $10FeCeO_2$ and $15FeCeO_2$, which suggests that additional reaction pathways may exist that lead to the formation of excess methane. Among the possible reaction pathways towards methane, propane decomposition to carbon deposits

$$C_3H_8 \rightarrow CH_4 + 2C_{(s)} + 2H_2 \quad (4)$$

is likely to occur at the temperature range of our experiments while the CO_2 methanation reaction[38]

$$CO_2 + 4H_2 \rightarrow CH_4 + 2H_2O \quad (5)$$

cannot be excluded. The former reaction is expected to severely affect the stability of these catalysts and will be discussed in more detail at a later section. However, the total selectivity to methane and ethylene decreases significantly at high Fe content indicating that these pathways do not dominate the catalytic performance under these reaction conditions.

The improved catalytic performance of the $10FeCeO_2$ and $15FeCeO_2$ catalysts is associated with the lower amount of other hydrocarbon by-products present under our reaction conditions. Considering that the overall carbon balance as calculated based on the total carbon flow of all gaseous reactants/products is usually above 98–99%, the rest of the carbon flow pertains to carbon oxides, CO and CO_2. It must be highlighted here that the majority of carbon oxides pertains to CO that is also consistent with previous reports.[23,25,39]

Although CO_2 formation from deep oxidation is plausible, CO_2 readily reacts over the catalytic surface under our reaction conditions as also shown in Fig. 2a. It is evident that the addition of Fe in ceria shows a monotonic increase in the apparent CO_2 conversion that resembles the propane conversion behavior. The maximum CO_2 conversion (~30%) was observed for the $15FeCeO_2$ catalyst. In the carbon dioxide assisted alkane oxidative dehydrogenation reaction it is well recognized that CO_2 participates mainly in the RWGS reaction which in turn favours propane conversion as discussed earlier. The catalytic behavior presented here for the Fe-doped catalysts appears to be consistent with the aforementioned reaction scheme, but the difference in product selectivity across different catalysts underscores the complexity of the reaction network that exists. In addition, recent report[38] also highlights the possibility of CO_2 participation in methanation (reaction (5)) as well as in propane dry reforming reaction (reaction (6)).

$$C_3H_8 + 3CO_2 \rightarrow 6CO + 4H_2 \quad (6)$$

Very recently, the concept of CO_2 dissociation over reduced metal oxides was also introduced in light of reoxidizing surface oxygen vacancies according to the following reaction.[40]

$$CO_2 + [*]_{vacancy} \rightarrow CO + [O*]_{lattice} \quad (7)$$

However, it is hard to clearly distinguish the actual selectivity to CO and/or CO_2 due to the uncertainty of the relative contribution of CO production from propane combustion, reverse water gas shift reaction, dry reforming, reverse Boudouard reaction or CO_2 splitting. Future experimental endeavours towards the establishment of kinetic and mechanistic understanding can shed light on the actual role of CO_2 on the activity, stability and/or deactivation of the catalyst reported herein.

Effect of temperature and residence time on catalytic activity

Next, we evaluate the effect of temperature as well as residence time on the catalytic performance of the most selective catalyst, $10FeCeO_2$. Specifically, we assess the catalyst activity in the 450–600 °C temperature range while we also varied the total flow of the reaction mixture within the 10–30 ml min^{-1} range. Fig. 3 compares the relevant results for the propane conversion as well as propylene selectivity and yield. The selectivity to other products is also shown in Fig. S3 of the ESI.† Upon increasing the temperature and/or reducing the residence time (W/F), the propane conversion increases significantly reaching a maximum of 52% at 600 °C and 0.33 $g_{cat.} \times h\ L^{-1}$. The selectivity

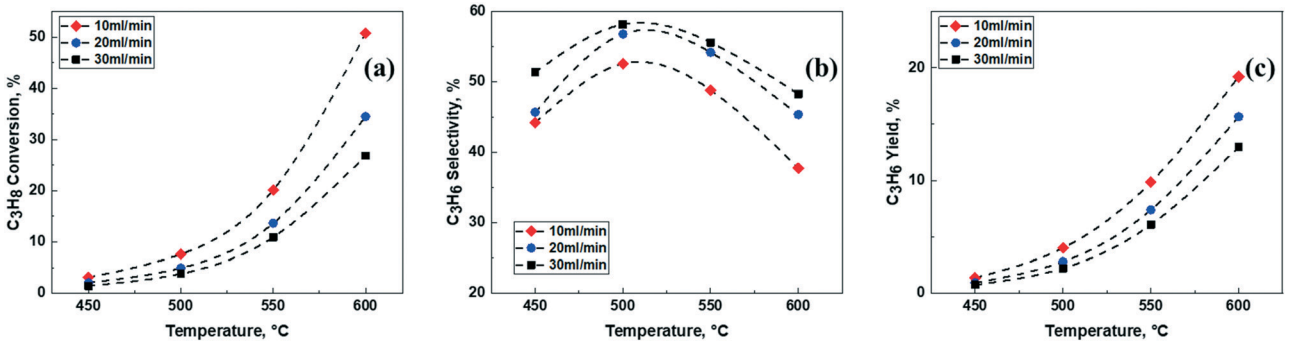

Fig. 3 Effect of temperature as well as residence time on (a) propane conversion, (b) propylene selectivity and (c) propylene yield of the most selective catalyst, 10FeCeO$_2$. Data pertain to initial reaction conditions.

to propylene is monotonically reduced upon increasing the residence time which is associated with consecutive paraffin/olefin oxidation to CO_x as also shown in Fig. S3.† The propylene selectivity reaches a maximum upon increasing the temperature around 500–550 °C while a decrease is observed at a higher temperature. The decrease in selectivity at high temperature is attributed to combustion to CO_x, thermal cracking of propane and consecutive oxidation of propylene by either catalyst surface oxygen species or carbon dioxide.[41] Thermodynamic analysis of standard Gibbs free energy change of light alkane and olefin cracking shows that spontaneity of olefin cracking outweigh alkane cracking, especially at high temperatures.[42] This is also consistent with our experimental results presented in the ESI† that show a monotonic increase in selectivity to ethylene and methane, the major products of C_3 cracking. It is very important here to underscore that propane cracking and overall catalyst deactivation can also be associated with the presence of acidic sites on the catalyst surface. In oxygen assisted alkane ODH it has been shown that the strength of Lewis acidity of the cation sites of the catalyst besides selective C–H activation also leads to non-selective activation and combustion. However, a study on Fe-doped CeO_2 catalysts with similar Fe loading has shown that even though the incorporation of Fe increases the amount of Brønsted and Lewis acids (as compared to the pure CeO_2 support), their intrinsic strength is relatively low as revealed by *in situ* IR coupled with NH_3-TPD.[43] Under similar reaction conditions, Nijhuis *et al.* reported the formation of coke deposits at different positions of the catalyst bed as revealed by *in situ* Raman and thermogravimetric studies. They found that significantly less coke was observed at the top catalyst layers than the middle and bottom parts of the catalyst bed.[44] promising propylene selectivity has been shown, next we evaluate the stability of all catalysts synthesized with time on streamSince the FeCe oxide catalysts showed promising propylene selectivity at 550 °C, next we evaluate at the same temperature the stability of all catalysts with time on stream.

Effect of C_3H_8/CO_2 in the feed on propane ODH

The effect of C_3H_8/CO_2 in the feed on the catalytic performance of the most selective catalyst identified, *i.e.* 10% FeCeO$_2$, was studied at 550 °C and a total flow of 20 ml min^{-1}. Relevant results concerning propane conversion and propylene selectivity are summarized in Fig. 4. Our data show that higher partial pressure of CO_2 in the feed mixture results in a slight decrease in conversion for feed rich in propane and almost no change for low propane initial concentration. In all cases, a marked decrease in propylene selectivity was observed. The highest propylene selectivity exceeded 60% for a 5 : 1 C_3H_8/CO_2 ratio in the reaction feed while the propane conversion was maintained at ~18% resulting in a maximum of ~11% propylene yield. On equimolar feed, the propylene selectivity remains the same while the propane conversion increases in the presence of dilute feed (1 : 1). These results in conjunction with the preceding discussion suggest that the observed negative effect of CO_2 on propylene selectivity could be attributed to the promotion in the propane dry reforming pathway.

Time-on-stream catalytic performance and deactivation

Fig. 5(a–c) show the propane conversion and selectivity of major products on three Fe-doped CeO_2 samples with time-

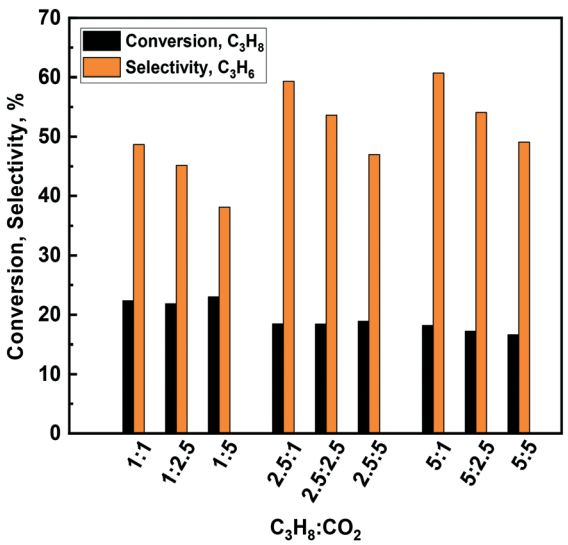

Fig. 4 Effect of propane and/or carbon dioxide partial pressure on the catalytic performance. Catalyst: 10FeCe600. Reaction conditions: 550 °C, 20 mL total flow, 200 mg catalyst loading.

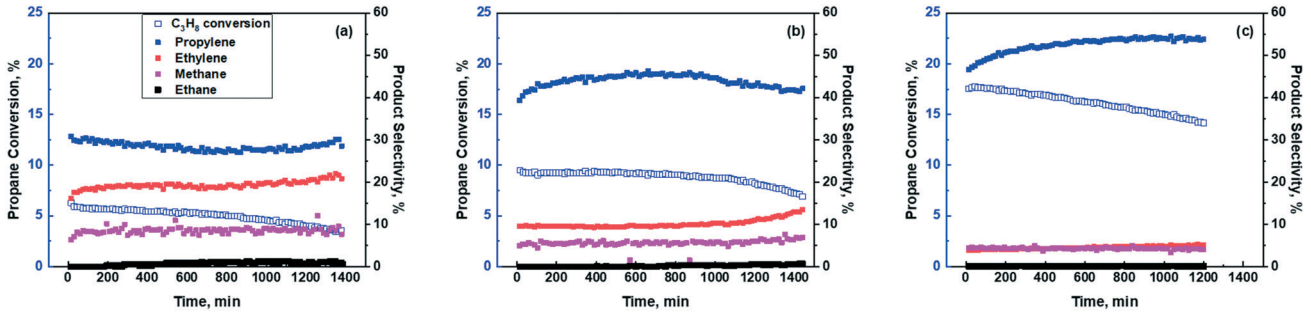

Fig. 5 Time-on-stream catalytic performance of (a) $1FeCeO_2$, (b) $5FeCeO_2$ and (c) $10FeCeO_2$ catalysts. Data pertain to 20 ml min^{-1} total flow (w/F = 0.6 g s cc^{-1}) and constant temperature at 550 °C.

on-stream (stability performance of all the rest of the catalysts is listed in the ESI,† Fig. S4). The stability of the catalysts was tested for 20–24 h time-on-stream. We observe that the selectivity to propylene appears to be stable for most of the catalytic materials tested. With a closer look at the Fe-doped catalysts with a large Fe/Ce ratio, an increase in propylene selectivity is observed within the first 2–4 hours of reaction and then remained stable. For the $10FeCeO_2$ catalyst, this increase was almost 10% and was accompanied by a gradual decrease in propane conversion from 17.5% to 14%. A similar behaviour was observed for the $15FeCeO_2$ catalyst. In contrast, for low Fe concentration catalysts, the propane conversion is more stable with time-on-stream; the best stability performance was observed for the $5FeCeO_2$ catalyst. More specifically, the conversion for the 1, 2.5 and $5FeCeO_2$ catalysts was found to be stable up to 6, 10 and 15 hours, respectively, while for the rest of the catalysts a monotonic decrease is observed.

It is worth mentioning here that for the low Fe concentration catalysts, the gradual decrease of propane conversion at very long time-on-stream is accompanied by a simultaneous increase in the selectivity of ethylene and methane. This result suggests that the observed deactivation is also associated probably with consecutive paraffin and/or olefin cracking that can lead to lighter hydrocarbons and/or coke. On the other hand, even though a monotonic decrease in propane conversion was observed for the catalysts with a large Fe/Ce ratio, no significant change was noticed in methane and ethylene selectivity. These results underscore that between the low and high Fe/Ce catalysts, different deactivation mechanisms may exist that directly affect the stability of their catalytic performance. In order to investigate the effect of CO_2 on the stability of our catalysts, experiments were also conducted in the absence of CO_2 in the reaction feed for the $10FeCeO_2$ catalysts and relevant results are shown in Fig. S5 of the ESI.† By comparing relevant catalytic results under identical reaction conditions, we observe an increase of the initial propane conversion when no CO_2 was present in the reaction feed while the initial propylene selectivity was almost the same. With time-on-stream, there is very rapid deactivation of the $10FeCeO_2$ catalyst as can be clearly seen from the monotonic and rapid drop in propane conversion. The rapid deactivation is accompanied by the simultaneous monotonic increase in the selectivity of ethylene indicating the presence of propane cracking among the primary pathways. It appears that the presence of CO_2 in the feed helps improve the stability performance of the catalysts probably due

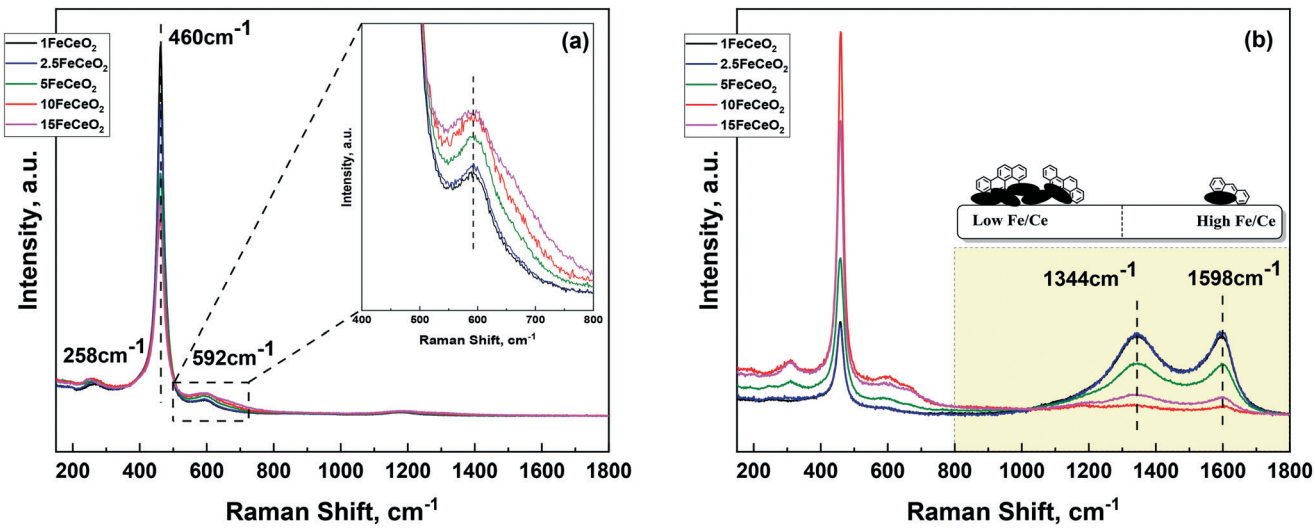

Fig. 6 Raman spectra of (a) fresh catalysts (inset shows the enlarged 400–800 cm^{-1} region) and (b) spent catalysts.

to the reoxidation of surface active sites and/or by *in situ* removal of coke deposits from the surface *via* the reverse Boudouard reaction. We believe that the initial improvement of propane conversion can be associated with the promotion of propane adsorption on all available and accessible active sites. This hypothesis is also in agreement with a recent study on $FeNi/CeO_2$ systems[25,45] where competitive adsorption between propane and CO_2 was highlighted among the key factors controlling the catalyst productivity.

To further investigate the reasons behind the observed deactivation, thorough characterization of the fresh and post reaction catalysts has been performed *via* Raman spectroscopy. Raman spectroscopy is a powerful tool for the structural characterization of metal oxides.[46,47] Fig. 6a shows the Raman spectra of the fresh catalysts after calcination. The spectral envelope in the 200–800 cm^{-1} range displays a very strong band located at 460 cm^{-1} which is associated with the F_{2g} vibrational mode of CeO_2.[48] Upon increasing of Fe, a very small shift was observed to lower wavenumbers that is ascribed to the gradual doping of the CeO_2 lattice with Fe and is consistent with the XRD results discussed in an earlier section. A closer look shows a monotonic increase in the intensity of the D band (Fig. 6a-inset) located at 592 cm^{-1} which is associated with the presence of substoichiometric CeO_{2-x} units underscoring an increase in oxygen vacancies.[49] The relative intensity ratio of 592 cm^{-1} and 460 cm^{-1}, I_{592}/I_{460}, has been routinely used in the open literature[50–52] as an indicator of the presence of oxygen vacancies in CeO_2 based materials. The I_{592}/I_{460} is shown in the ESI,† Fig. S6. We observe that the I_{592}/I_{460} reaches a maximum at high Fe/Ce. This trend resembles the increase in propylene selectivity thus suggesting the possible participation of the oxygen deficient site in the selective dehydrogenation pathway. On the other hand, post-reaction Raman characterization shown in Fig. 6b, show the presence of two broad and intense peaks located at 1344 cm^{-1} and 1598 cm^{-1} which are associated with the G and D bands of carbon deposits.[7,53,54] At low Fe/Ce, coke is favoured while at high Fe/Ce coke is minimal. This result suggests that the gradual deactivation of the low Fe/Ce catalysts is due to the formation of carbon deposits on the surface which is also consistent with the increased selectivity towards cracking products as discussed earlier. However, one cannot exclude the possible reactivity loss due to the rapid reduction of available active sites under these reaction conditions. It has been shown that a small amount of Fe incorporation in CeO_2 lowers the reduction temperature of the main surface oxygen sites from ~520 °C to the range of 370–400 °C indicating weakening of surface Ce–O bonds that leads to an enhanced oxygen mobility. Although H_2-TPR/O_2-TPO experimentation has shown to be a valuable tool towards understanding the redox properties of Fe-doped CeO_2 catalysts,[43,55,56] future research endeavors towards an in-depth investigation of cyclic H_2-TPR and CO_2-TPO experiments can provide insights into the product distribution and contribution of CO_2 as an oxidizing agent. Coupling these measurements with advanced *operando* spectroscopic techniques such as Raman and IR can disentangle the contribution of individual active sites to the overall performance while providing at the same time molecular level information on catalyst deactivation.

In addition, *ex situ* XPS was applied to investigate the chemical states of highly ordered carbon nanostructures deposited over fresh and spent iron–cerium oxides. A symmetrical sp^3 peak (284.6–284.8 eV) and an asymmetrical sp^2 peak (284.2–284.3 eV) were fitted to the C1s main feature for post-reaction catalysts.[57] The detailed deconvolution is shown in the ESI† (Fig. S7). An apparent increase was observed in the C/O ratio for up to $5FeCeO_2$ spent catalysts as opposed to the fresh material, where the C/O basis was estimated within 20–30%. A major contribution of this carbon amount lies in the advent of the sp^2 peak fitted on the basis of the invariant sp^3 peak, revealing aromatic structures as the primary chemical states of coke. As higher Fe-dopant concentration was reached, the C/O ratio decreases together with the sp^2 peak area percentage, observation that is consistent with our Raman data. Particularly, the C/O ratio fell within the range of that of the reference fresh material, which is a strong proof of minor carbon deposition after 24 hour ODH reaction. Although the suppressed formation of coke deposits appears to be associated with the higher propylene selectivity observed, the reasons behind the monotonic decrease in the conversion for the high Fe/Ce catalysts is still elusive.

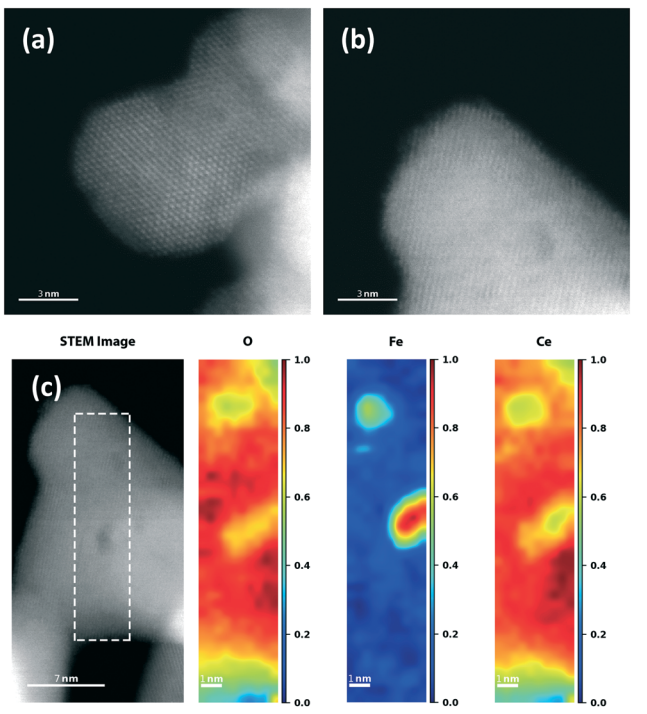

Fig. 7 High resolution STEM images of the 10% $FeCeO_2$ catalyst particles before (a) and after (b) reaction. (c) The dashed box indicates the element mapping area and its corresponding oxygen, iron, and cerium distribution maps.

In an effort to gain more insight into the observed catalytic behaviour of $10FeCeO_2$, the samples before and after reaction were investigated using a scanning transmission electron microscope (STEM). Typical catalyst particles before and after the reaction are shown in Fig. 7(a–c). It is observed that the particle size before the reaction is less than 10 nm (consistent with the XRD results) while the particle size after the reaction is in general larger than 15 nm. This result points to the decrease in the specific surface area due to sintering as one possible reason behind the observed catalyst deactivation as seen from the conversion of propane in time-on-stream. In addition, element mapping was carried out for the after-reaction sample. As shown in Fig. 7c, iron is found in two localized areas in the mapped area. The result suggests that, besides CeO_2 sintering, iron also migrates to localized areas instead of keeping its initial solid solution form during the reaction indicating a significant change in morphology of the catalysts which can in turn affect the overall catalytic performance.

Conclusions

The CO_2-assisted propane oxidative dehydrogenation reaction was tested over a series of Fe-doped cerium oxide catalysts with various Fe/Ce ratios from 1% to 15%. It is demonstrated that both propane conversion and propylene selectivity were improved at higher Fe/Ce ratio, indicating that the propane ODH pathway is favored over Fe-rich surfaces. Careful examination on reaction by-products revealed propane cracking and dry reforming as the two major side reactions in the reaction system. At high Fe/Ce ratio, cracking reactions appear to be minimized. In general, all catalysts exhibit comparably stable catalytic behavior for over 20 hours of continuous catalytic test, with $5FeCeO_2$ standing out as the most stable catalyst. Raman, XPS and STEM characterization of post-reaction catalysts was performed in order to study the possible reasons for $xFeCeO_2$ catalyst deactivation. Our characterization results unveiled that at low Fe/Ce ratio, carbon deposition and coke formation are the primary reasons that hamper propane conversion while at high Fe/Ce ratio, the $FeCeO_2$ catalysts suffer from ceria crystal sintering and Fe migration to form nanosize crystals.

Conflicts of interest

There are no conflicts to declare.

Acknowledgements

This material is based upon work supported in part by Rutgers, The State University of New Jersey, and the National Science Foundation Award #1751683. The authors would like to thank Prof. A. Neimark and Prof. T. Asefa for helping with the BET measurements and porosity analysis, Prof. P. Batson and Dr. Y. Yeh for the STEM images and Dr. W. Zheng for the XPS data.

Notes and references

1 C. A. Gärtner, A. C. van Veen and J. A. Lercher, Oxidative Dehydrogenation of Ethane: Common Principles and Mechanistic Aspects, *ChemCatChem*, 2013, **5**(11), 3196–3217.
2 C. A. Carrero, R. Schloegl, I. E. Wachs and R. Schomaecker, Critical Literature Review of the Kinetics for the Oxidative Dehydrogenation of Propane over Well-Defined Supported Vanadium Oxide Catalysts, *ACS Catal.*, 2014, **4**(10), 3357–3380.
3 F. Cavani, N. Ballarini and A. Cericola, Oxidative dehydrogenation of ethane and propane: How far from commercial implementation?, *Catal. Today*, 2007, **127**(1–4), 113–131.
4 B. V. Vora, Development of Dehydrogenation Catalysts and Processes, *Top. Catal.*, 2012, **55**(19–20), 1297–1308.
5 V. Blay, E. Epelde, R. Miravalles and L. A. Perea, Converting olefins to propene: Ethene to propene and olefin cracking, *Catal. Rev.: Sci. Eng.*, 2018, **60**(2), 278–335.
6 L. Sun, Y. Chai, W. Dai, G. Wu, N. Guan and L. Li, Oxidative dehydrogenation of propane over Pt–Sn/Si-beta catalysts: key role of Pt–Sn interaction, *Catal. Sci. Technol.*, 2018, **8**(12), 3044–3051.
7 Q. Li, Z. Sui, X. Zhou, Y. Zhu, J. Zhou and D. Chen, Coke Formation on Pt–Sn/Al2O3 Catalyst in Propane Dehydrogenation: Coke Characterization and Kinetic Study, *Top. Catal.*, 2011, **54**(13–15), 888–896.
8 S. Kawi and Y. Kathiraser, CO2 as an oxidant for high-temperature reactions, *Front. Energy Res.*, 2015, **3**, 13.
9 M. A. Botavina, Y. A. Agafonov, N. A. Gaidai, E. Groppo, V. Cortés Corberán, A. L. Lapidus and G. Martra, Towards efficient catalysts for the oxidative dehydrogenation of propane in the presence of CO2: Cr/SiO2 systems prepared by direct hydrothermal synthesis, *Catal. Sci. Technol.*, 2016, **6**(3), 840–850.
10 K. Takehira, Y. Ohishi, T. Shishido, T. Kawabata, K. Takaki, Q. Zhang and Y. Wang, Behavior of active sites on Cr-MCM-41 catalysts during the dehydrogenation of propane with CO2, *J. Catal.*, 2004, **224**(2), 404–416.
11 D. Yun, J. Baek, Y. Choi, W. Kim, H. J. Lee and J. Yi, Promotional Effect of Ni on a CrOxCatalyst Supported on Silica in the Oxidative Dehydrogenation of Propane with CO2, *ChemCatChem*, 2012, **4**(12), 1952–1959.
12 J. Baek, H. J. Yun, D. Yun, Y. Choi and J. Yi, Preparation of Highly Dispersed Chromium Oxide Catalysts Supported on Mesoporous Silica for the Oxidative Dehydrogenation of Propane Using CO2: Insight into the Nature of Catalytically Active Chromium Sites, *ACS Catal.*, 2012, **2**(9), 1893–1903.
13 P. Michorczyk, P. Pietrzyk and J. Ogonowski, Preparation and characterization of SBA-1–supported chromium oxide catalysts for CO2 assisted dehydrogenation of propane, *Microporous Mesoporous Mater.*, 2012, **161**, 56–66.
14 P. Michorczyk, J. Ogonowski and K. Zeńczak, Activity of chromium oxide deposited on different silica supports in the dehydrogenation of propane with CO2 – A comparative study, *J. Mol. Catal. A: Chem.*, 2011, **349**(1–2), 1–12.

15 A. Burri, M. A. Hasib, Y.-H. Mo, B. M. Reddy and S.-E. Park, An Efficient Cr-TUD-1 Catalyst for Oxidative Dehydrogenation of Propane to Propylene with CO2 as Soft Oxidant, *Catal. Lett.*, 2017, **148**(2), 576–585.
16 M. Botavina, C. Barzan, A. Piovano, L. Braglia, G. Agostini, G. Martra and E. Groppo, Insights into Cr/SiO2 catalysts during dehydrogenation of propane: an operando XAS investigation, *Catal. Sci. Technol.*, 2017, **7**(8), 1690–1700.
17 P. Michorczyk, J. Ogonowski and M. Niemczyk, Investigation of catalytic activity of CrSBA-1 materials obtained by direct method in the dehydrogenation of propane with CO2, *Appl. Catal., A*, 2010, **374**(1–2), 142–149.
18 Q. Zhu, M. Takiguchi, T. Setoyama, T. Yokoi, J. N. Kondo and T. Tatsumi, Oxidative Dehydrogenation of Propane with CO2 Over Cr/H[B]MFI Catalysts, *Catal. Lett.*, 2011, **141**, 670–677.
19 Y. A. Agafonov, N. A. Gaidai and A. L. Lapidus, Influence of the preparation conditions for catalysts CrOx/SiO2 on their efficiency on propane dehydrogenation in the presence of CO2, *Russ. Chem. Bull.*, 2014, **63**, 381–388.
20 F. Zhang, R. Wu, Y. Yue, W. Yang, S. Gu, C. Miao, W. Hua and Z. Gao, Chromium oxide supported on ZSM-5 as a novel efficient catalyst for dehydrogenation of propane with CO2, *Microporous Mesoporous Mater.*, 2011, **145**(1–3), 194–199.
21 B. Yan, S. Yao, S. Kattel, Q. Wu, Z. Xie, E. Gomez, P. Liu, D. Su and J. G. Chen, Active sites for tandem reactions of CO2 reduction and ethane dehydrogenation, *Proc. Natl. Acad. Sci. U. S. A.*, 2018, **115**(33), 8278–8283.
22 E. Gomez, B. Yan, S. Kattel and J. G. Chen, Carbon dioxide reduction in tandem with light-alkane dehydrogenation, *Nat. Rev. Chem.*, 2019, **3**, 638–649.
23 E. Gomez, S. Kattel, B. Yan, S. Yao, P. Liu and J. G. Chen, Combining CO2 reduction with propane oxidative dehydrogenation over bimetallic catalysts, *Nat. Commun.*, 2018, **9**(1), 1398.
24 B. Yan, X. Yang, S. Yao, J. Wan, M. Myint, E. Gomez, Z. Xie, S. Kattel, W. Xu and J. G. Chen, Dry Reforming of Ethane and Butane with CO2 over PtNi/CeO2 Bimetallic Catalysts, *ACS Catal.*, 2016, **6**(11), 7283–7292.
25 E. Gomez, Z. H. Xie and J. G. G. Chen, The effects of bimetallic interactions for CO2-assisted oxidative dehydrogenation and dry reforming of propane, *AIChE J.*, 2019, **65**(8), e16670.
26 B. H. Yan, S. Y. Yao and J. G. G. Chen, Effect of Oxide Support on Catalytic Performance of FeNi-based Catalysts for CO2-assisted Oxidative Dehydrogenation of Ethane, *ChemCatChem*, 2020, **12**(2), 494–503.
27 C. T. Campbell and C. H. F. Peden, Oxygen Vacancies and Catalysis on Ceria Surfaces, *Science*, 2005, **309**(5735), 713–714.
28 F. J. Perez-Alonso, M. Lopez Granados, M. Ojeda, P. Terreros, S. Rojas, T. Herranz and J. L. G. Fierro, Chemical Structures of Coprecipitated Fe-Ce Mixed Oxides, *Chem. Mater.*, 2005, **17**, 2329–2339.
29 P. Michorczyk, P. Kustrowski, L. Chmielarz and J. Ogonowski, Influence of redox properties on the activity of iron oxide catalysts in dehydrogennation of propane with CO2, *React. Kinet. Catal. Lett.*, 2004, **82**, 121–130.
30 J. Kowalska-Kuś, A. Held and K. Nowińska, Oxydehydrogenation of C2–C4hydrocarbons over Fe-ZSM-5 zeolites with N2O as an oxidant, *Catal. Sci. Technol.*, 2013, **3**(2), 508–518.
31 J. R. Scheffe and A. Steinfeld, Oxygen exchange materials for solar thermochemical splitting of H2O and CO2: a review, *Mater. Today*, 2014, **17**(7), 341–348.
32 V. V. Galvita, H. Poelman, V. Bliznuk, C. Detavernier and G. B. Marin, CeO2-Modified Fe2O3 for CO2 Utilization via Chemical Looping, *Ind. Eng. Chem. Res.*, 2013, **52**(25), 8416–8426.
33 S. K. Sahoo, M. Mohapatra, B. Pandey, H. C. Verma, R. P. Das and S. Anand, Preparation and characterization of α-Fe2O3–CeO2 composite, *Mater. Charact.*, 2009, **60**(5), 425–431.
34 K. Li, H. Wang, Y. Wei and D. Yan, Direct conversion of methane to synthesis gas using lattice oxygen of CeO2–Fe2O3 complex oxides, *Chem. Eng. J.*, 2010, **156**(3), 512–518.
35 A. F. Rossi, N. Amaral-Silva, R. C. Martins and R. M. Quinta-Ferreira, Heterogeneous Fenton using ceria based catalysts: effects of the calcination temperature in the process efficiency, *Appl. Catal., B*, 2012, **111–112**, 254–263.
36 H.-X. Fan, J. Feng and W.-Y. Li, Promotional effect of oxygen storage capacity on oxy-dehydrogenation of ethylbenzene with CO2 over κ-Ce2Zr2O8(111), *Appl. Surf. Sci.*, 2019, **486**, 411–419.
37 Z. H. Gu, K. Z. Li, S. Qing, X. Zhu, Y. G. Wei, Y. T. Li and H. Wang, Enhanced reducibility and redox stability of Fe2O3 in the presence of CeO2 nanoparticles, *RSC Adv.*, 2014, **4**(88), 47191–47199.
38 A. Cárdenas-Arenas, A. Quindimil, A. Davó-Quiñonero, E. Bailón-García, D. Lozano-Castelló, U. De-La-Torre, B. Pereda-Ayo, J. A. González-Marcos, J. R. González-Velasco and A. Bueno-López, Isotopic and in situ DRIFTS study of the CO2 methanation mechanism using Ni/CeO2 and Ni/Al2O3 catalysts, *Appl. Catal., B*, 2020, **265**, 118538.
39 M. A. Atanga, F. Rezaei, A. Jawad, M. Fitch and A. A. Rownaghi, Oxidative dehydrogenation of propane to propylene with carbon dioxide, *Appl. Catal., B*, 2018, **220**, 429–445.
40 E. Nowicka, C. Reece, S. M. Althahban, K. M. H. Mohammed, S. A. Kondrat, D. J. Morgan, Q. He, D. J. Willock, S. Golunski, C. J. Kiely and G. J. Hutchings, Elucidating the Role of CO2 in the Soft Oxidative Dehydrogenation of Propane over Ceria-Based Catalysts, *ACS Catal.*, 2018, **8**(4), 3454–3468.
41 Z. Xie, Y. Ren, J. Li, Z. Zhao, X. Fan, B. Liu, W. Song, L. Kong, X. Xiao, J. Liu and G. Jiang, Facile in situ synthesis of highly dispersed chromium oxide incorporated into mesoporous ZrO2 for the dehydrogenation of propane with CO2, *J. Catal.*, 2019, **372**, 206–216.
42 X. Du, B. Yao, S. Gonzalez-Cortes, V. L. Kuznetsov, H. AlMegren, T. Xiao and P. P. Edwards, Catalytic dehydrogenation of propane by carbon dioxide: a medium-

temperature thermochemical process for carbon dioxide utilisation, *Faraday Discuss.*, 2015, **183**, 161–176.

43 Y. Peng, W. W. Yu, W. K. Su, X. Huang and J. H. Li, An experimental and DFT study of the adsorption and oxidation of NH3 on a CeO2 catalyst modified by Fe, Mn, La and Y, *Catal. Today*, 2015, **242**, 300–307.

44 T. A. Nijhuis, S. J. Tinnemans, T. Visser and B. M. Weckhuysen, Towards real-time spectroscopic process control for the dehydrogenation of propane over supported chromium oxide catalysts, *Chem. Eng. Sci.*, 2004, **59**(22–23), 5487–5492.

45 E. Gomez, S. Kattel, B. H. Yan, S. Y. Yao, P. Liu and J. G. G. Chen, Combining CO2 reduction with propane oxidative dehydrogenation over bimetallic catalysts, *Nat. Commun.*, 2018, **9**, 1398.

46 G. Tsilomelekis and S. Boghosian, Structural and vibrational properties of molybdena catalysts supported on alumina and zirconia studied by in situ Raman and FTIR spectroscopies combined with 18O/16O isotopic substitution, *Catal. Today*, 2010, **158**(1–2), 146–155.

47 A. Tribalis, G. D. Panagiotou, G. Tsilomelekis, A. G. Kalampounias, K. Bourikas, C. Kordulis, S. Boghosian and A. Lycourghiotis, Temperature-Dependent Evolution of the Molecular Configuration of Oxo-Tungsten(VI) Species Deposited on the Surface of Titania, *J. Phys. Chem. C*, 2014, **118**(21), 11319–11332.

48 B. Penkala, D. Aubert, H. Kaper, C. Tardivat, K. Conder and W. Paulus, The role of lattice oxygen in CO oxidation over Ce18O2-based catalysts revealed under operando conditions, *Catal. Sci. Technol.*, 2015, **5**(10), 4839–4848.

49 W. Huang and Y. Gao, Morphology-dependent surface chemistry and catalysis of CeO2nanocrystals, *Catal. Sci. Technol.*, 2014, **4**(11), 3772–3784.

50 Z. Wu, A. J. Rondinone, I. N. Ivanov and S. H. Overbury, Structure of Vanadium Oxide Supported on Ceria by Multiwavelength Raman Spectroscopy, *J. Phys. Chem. C*, 2011, **115**(51), 25368–25378.

51 M.-F. Luo, Z.-L. Yan, L.-Y. Jin and M. He, Raman Spectroscopic Study on the Structure in the Surface and the Bulk Shell of CexPr1-xO2-δ Mixed Oxides, *J. Phys. Chem. B*, 2006, **110**, 13068–13071.

52 M. Ridwan, R. Tamarany, J. Han, S. W. Nam, H. C. Ham, J. Y. Kim, S. H. Choi, S. C. Jang and C. W. Yoon, Atomically dispersed Cu on Ce1−xRExO2−δ nanocubes(RE = La and Pr) for water gas shift: influence of OSC on catalysis, *RSC Adv.*, 2015, **5**(109), 89478–89481.

53 H. An, F. Zhang, Z. Guan, X. Liu, F. Fan and C. Li, Investigating the Coke Formation Mechanism of H-ZSM-5 during Methanol Dehydration Using Operando UV–Raman Spectroscopy, *ACS Catal.*, 2018, **8**(10), 9207–9215.

54 I. Pocsik, M. Hundhausen, M. Koos and L. Ley, Origin of the D peak in the Raman spectrum of microcrystalline graphite, *J. Non-Cryst. Solids*, 1998, **227–230**, 1083–1086.

55 K. Z. Li, M. Haneda, P. H. Ning, H. Wang and M. Ozawa, Microstructure and oxygen evolution of Fe-Ce mixed oxides by redox treatment, *Appl. Surf. Sci.*, 2014, **289**, 378–383.

56 Z. L. Zhang, D. Han, S. J. Wei and Y. X. Zhang, Determination of active site densities and mechanisms for soot combustion with O-2 on Fe-doped CeO2 mixed oxides, *J. Catal.*, 2010, **276**(1), 16–23.

57 R. Blume, D. Rosenthal, J.-P. Tessonnier, H. Li, A. Knop-Gericke and R. Schlögl, Characterizing Graphitic Carbon with X-ray Photoelectron Spectroscopy: A Step-by-Step Approach, *ChemCatChem*, 2015, **7**(18), 2871–2881.

